https://doi.org/10.5194/egusphere-2026-4159
Preprint. Discussion started: 13 August 2026

Linking cloud hydrometeor growth and surface precipitation to synoptic forcing at Dumont d'Urville, East Antarctica

AV Sreenath[1,2], Peter T May[1], Steven Siems[1,2], Heather Corden[3], and Alexis Berne[3]
[1]School of Earth, Atmosphere and Environment, Monash University, Melbourne, Victoria, Australia
[2]Australian Research Council's Securing Antarctica's Environmental Future (SAEF), Melbourne, Victoria, Australia
[3]Environmental Remote Sensing Laboratory, Swiss Federal Institute of Technology in Lausanne, Lausanne, Switzerland.
Correspondence: AV Sreenath (sreenath.av@monash.edu)

Abstract.

We investigate how weather regimes influence surface precipitation and associated cloud microphysical processes at Dumont d'Urville (DDU; 66.7° S, 140.0° E) using data from the Antarctic Precipitation: Remote Sensing from Surface and Space (APRES3) project. Two precipitation-producing regimes, Summer Warm Air Advection (S-WAA) and Low-Pressure (Low-P), account for 94.2% of total precipitation at DDU. Hydrometeor growth processes were analysed through comprehensive case studies of Low-P and S-WAA events. The polarimetric signatures during the Low-P event indicate riming and secondary ice production (SIP) within the -10 to $-14\,^{\circ}$C layer (2–3.5 km), which falls within the dendritic growth zone (DGZ; -10 to $-20\,^{\circ}$C). Riming intensifies between 1 and 2 km (-7 to $-10\,^{\circ}$C), whereas below 1 km, downslope flow leads to pronounced hydrometeor sublimation and sublimation-induced SIP. Thus, the surface precipitation associated with this event displays an intermittent pattern, with a predominance of graupel. In contrast, the S-WAA regime is associated with a moist boundary layer, favouring persistent surface precipitation. The polarimetric signatures in the upper half of the DGZ (-14 to -20°C, 2.5–3.5 km) suggest hydrometeor growth through vapour deposition, while signatures below down to 1 km (-8 to -14°C) align with aggregation processes. Enhanced riming and SIP driven by the Hallett–Mossop process are observed below 1 km. Our findings emphasise that synoptic weather regimes primarily impact precipitation growth, while boundary-layer flow and moisture play a significant role in snowfall efficiency at DDU in East Antarctica.

1 Introduction

Changes in snowfall accumulation are a primary driver of the Antarctic Ice Sheet's surface mass balance, resulting in both immediate and delayed impacts on global mean sea level (Boening et al., 2012; Hansen et al., 2016; Ligtenberg et al., 2013; Medley and Thomas, 2019). Observations from polar-orbiting satellites show a mean snowfall rate of approximately 171 mm water equivalent per year north of 81° S (Palerme et al., 2014). However, surface precipitation varies significantly across the continent and by meteorological state, with relatively high precipitation along coastal margins, where annual totals can reach several tens of centimetres, and it may exceed meters in some locations (Milani et al., 2018; Lemonnier et al., 2020).

Precipitation over the Antarctic domain increased during the 20$^{\text{th}}$ century, mainly associated with changes in southern-hemisphere circulation patterns and short-term variations associated with extreme precipitation events (Marshall et al., 2017;

Bodart and Bingham, 2019; Turner et al., 2019; Kim et al., 2020). On average, models from the Coupled Model Intercomparison Project Phase 5 (CMIP5) simulate an increase in Antarctic precipitation of approximately 5.5-24.5% between 1986–2005 and 2080–2099, depending on the greenhouse gas emission scenario considered (Palerme et al., 2017). At multi-decadal timescales, changes to synoptic-scale circulation patterns account for the recent and projected increases in Antarctic snow accumulation (Dalaiden et al., 2020). Coastal winds exert strong control over snowfall variability in Antarctica by influencing regional circulation patterns and moisture availability (Mathiot et al., 2012; Dale et al., 2016; Silvano et al., 2020). Studies have reported that the interplay between local temperature inversions and synoptic pressure gradients exerts primary control on extreme wind patterns over Antarctica (Parish and Bromwich, 2007; Turner et al., 2009). Such multi-scale interactions modulate boundary-layer structure, moisture transport, cloud growth and precipitation formation (Hofer et al., 2021; Gehring et al., 2022; Silva et al., 2023).

Spaceborne analyses show that nearly 60% of global precipitation is developing through the ice phase (Heymsfield et al., 2020). The ice crystals undergo various microphysical processes during their fall to the ground, including riming, aggregation, vapour deposition and melting (Pruppacher et al., 1998; Lawson and Gettelman, 2014; DeLaFrance et al., 2024). The collisions between ice crystals and supercooled liquid droplets are called riming, which results in the formation of denser graupel-like hydrometeors with enhanced fall velocities (Kumjian et al., 2016). Aggregation involves collisions and adhesion among multiple ice crystals, forming larger ice aggregates (Field et al., 2017). The ice crystal growth processes, including riming, aggregation and vapour deposition, are reflected in radar observables such as reflectivity (Z_{H}), differential reflectivity (Z_{DR}), specific differential phase (K_{DP}) and copolar correlation coefficient (ρ_{HV}) (Moisseev et al., 2015; Schneebeli et al., 2013; Pfitzenmaier et al., 2018). Riming and aggregation can lead to similar polarimetric signatures with increased Z_{H} and decreased Z_{DR} towards the surface (Kumjian et al., 2022); however, rimed hydrometeors show higher fall speeds than unrimed particles with the same maximum dimension (Locatelli and Hobbs, 1974). The temperature range of -20 to -10°C is favourable for the formation of dendrites and other planar crystal growth, and is typically referred to as the dendritic growth zone (DGZ). The depositional growth rate peaks at -15°C, where dendritic particles can exceed 1.5 mm in size within 10 min of growth time at liquid-water saturation (Takahashi, 2014). Aggregation in the DGZ can be detected by radar polarimetry as a reduction in Z_{DR} and a concurrent increase in radar reflectivity (Kumjian, 2013). Mainly, the branched morphology of dendritic crystals promotes interlocking and enhances their tendency to stick together, favouring aggregate formation (Connolly et al., 2012).

Despite their significant role in regulating the global climate, precipitation processes remain poorly constrained over Antarctica due to the lack of reliable in situ observations under harsh environmental conditions (Listowski and Lachlan-Cope, 2017; Lawson and Gettelman, 2014; Pei et al., 2025). The limited observational coverage over this region leads to uncertainties in the representation of mixed-phase clouds in climate models, further resulting in the underestimation of the low-level cloud fraction and supercooled liquid water (Bodas-Salcedo et al., 2016; Pei et al., 2023; Vignon et al., 2021). Thus, an improved understanding of the interactions among the synoptic-scale circulation, local winds, and cloud processes is essential to improve simulations of Antarctic precipitation, particularly given the persistent biases in the vertical structure of snowfall reported in previous studies (Grazioli et al., 2017b).

https://doi.org/10.5194/egusphere-2026-4159
Preprint. Discussion started: 13 August 2026

In recent years, several dedicated observational campaigns have been conducted to reduce long-standing gaps in our understanding of cloud and precipitation processes across the Antarctic continent. These efforts include comprehensive measurements at Dumont d'Urville (DDU), Davis and Princess Elisabeth stations (Ferrone and Berne, 2023; Wiener et al., 2024; Genthon et al., 2018; Alexander et al., 2023; Di Natale et al., 2022). In this study, we analyse observational data collected between 2015 and 2023 at DDU (66.7°S, 140.0°E) as part of the Antarctic Precipitation: Remote Sensing from Surface and Space (APRES3) project (Genthon et al., 2018). Drawing on the integrated ground-based observations from the APRES3 project, this study investigates the following question: How does synoptic forcing influence cloud hydrometeor growth and surface precipitation at Dumont d'Urville, East Antarctica? To address this question, we first identify the precipitation-bearing weather regimes at DDU and then analyse the microphysics of hydrometeor growth and surface precipitation in these regimes through two detailed case studies.

The paper is organised as follows. Section 2 describes the observational and reanalysis datasets and the methods employed. Section 3 presents the results, including the characteristics of the synoptic regimes and detailed case studies of two precipitation-bearing regimes, emphasising their vertical precipitation structure and hydrometeor growth processes. Section 4 summarises the findings and provides concluding remarks.

2 Data and methods

2.1 MRR data

The Micro Rain Radar (MRR; Metek MRR-2) has operated at DDU since November 2015 as part of the APRES3 project (Genthon et al., 2018). Operating at 24 GHz (K-band), the MRR provides vertical profiles of equivalent reflectivity (Z_e), Doppler velocity (W), and spectral width (σ), which are used in this study to characterise precipitation structure. It provides data at 100 m vertical resolution from 300 to 3000 m above sea level. The quality-controlled MRR data are available at a 1-minute temporal resolution, with raw observations processed using the methodology of Maahn and Kollias (2012). A detailed overview of the radar configuration and data pre-processing procedures are provided by Grazioli et al. (2017a) and Genthon et al. (2018). At DDU station, the MRR is housed within a radome. Comparisons of co-located X-band radar and a temporarily deployed second MRR outside the radome (Grazioli et al., 2017a; Durán-Alarcón et al., 2019) indicate that the radome-enclosed MRR systematically underestimates reflectivity by nearly 6 dBZ. Accordingly, all MRR equivalent reflectivity data used in this study were corrected by adding 6 dBZ, consistent with the methodology of Wiener et al. (2024) for the same instrument.

2.2 Snow gauge data

The OTT Pluvio^2 measures the amount of snowfall falling into the bucket by weighing it and converting it to mm water equivalent (Wiener et al., 2024). The Pluvio^2 measured surface precipitation data are available from November 2015 to April 2023 with 1-minute temporal resolution. Detailed explanations of the instrumentation and data processing are available from Grazioli et al. (2017a) and Genthon et al. (2018). Following Grazioli et al. (2017a), MRR reflectivity at the lowest range gate,

https://doi.org/10.5194/egusphere-2026-4159
Preprint. Discussion started: 13 August 2026

together with near-surface wind speed, was used to identify the periods of actual cloud precipitation and to exclude spurious gauge accumulation caused by wind-blown snow. Time steps with no valid MRR signal at the lowest available range gate (300 m) were classified as precipitation-free and excluded from the analysis, including periods when the 10 m wind speed exceeded 15 ms^{-1}. Under these conditions, increases in the Pluvio^2 record presumably resulted from spurious accumulation caused by blowing snow or mechanical effects on the gauge, rather than from actual precipitation, and were excluded from the analysis. To ensure consistency with the ERA5 wind speed data, the precipitation observations and MRR measurements were resampled to an hourly resolution.

2.3 MXPol radar

The mobile X-band dual-polarisation radar (MXPol) was deployed at DDU during a summer campaign from 7 December 2015 to 31 January 2016 (Grazioli et al., 2017a; Genthon et al., 2018). It operated at 9.41 GHz and had a 3dB beamwidth of 1.4 degrees. The radar provides a radial resolution of 75 m and a maximum measurement range of 30 km. Its primary operation used a five-minute scan, consisting of plan position indicator (PPI) scans and range height indicator (RHI) scans. RHI scans from the MXPol radar performed at a fixed azimuth of 293° were used to obtain reflectivity (Z_{H}), differential reflectivity (Z_{DR}), specific differential phase (K_{DP}), and the correlation coefficient (ρ_{HV}) for the periods 00:00–03:00 UTC on 29 December 2015 and 28 January 2016. Only observations collected at elevation angles below 40° are considered to minimise the influence of elevation-dependent biases on the polarimetric variables (Ryzhkov et al., 2005; Dedekind et al., 2023). PPI scans with a fixed elevation angle of 5° are used to derive the horizontal wind using the Velocity Azimuth Display (VAD) method in the Py-ART framework. As VAD combines radial velocities measured around an azimuthal circle to estimate a mean wind vector, the retrieval assumes that horizontal variations within the sampled area are sufficiently small. The radial velocity varies sinusoidally with azimuth angle and can be expressed as:

$$V_r(\theta) = \frac{a_0}{2} + \sum_{n=1}^{N} a_n \cos(n\theta) + \sum_{n=1}^{N} b_n \sin(n\theta) \tag{1}$$

where Vr is the radial velocity, θ is the azimuth angle, and an and bn are the Fourier coefficients (Browning and Wexler, 1968; Holleman, 2005).

A spectrogram analysis was performed using spectral reflectivity as a function of Doppler velocity and height derived from the vertical-pointing mode of X-band radar. The processed radar dataset provides Doppler spectra sampled using 256 FFT bins, covering a Doppler velocity range of -9.96 to 9.96 m s^{-1}.

2.4 Multi-angle snowflake camera (MASC)

The MASC observation data is available from November 2015 to January 2016. The instrument consists of three high-resolution coplanar cameras that share a common focal point and are separated by approximately 10 cm, enabling the acquisition of stereoscopic images of individual snowflakes (Garrett et al., 2012). In this study, we use the probabilistic classification of hydrometeor types derived from MASC observations following Praz et al. (2017). The relative contribution of each

https://doi.org/10.5194/egusphere-2026-4159
Preprint. Discussion started: 13 August 2026

hydrometeor type—small particles (SP), columnar crystals (CC), planar crystals (PC), aggregates (AG), graupel (GR), and a combination of columnar and planar crystals (CPC)—is estimated from the MASC probabilistic classification. The class probabilities are summed over all records within a given time window, and each class sum is normalised by the total probability. In this analysis, the SP category is excluded, and the remaining class contributions are re-normalised such that their sum equals unity. More information on the instrument design, operation, and data processing is provided in Grazioli et al. (2022).

2.5 Radiosonde observations

Radiosonde observations from Météo-France at DDU station were used to generate Skew-T log-p diagrams for 00:00 UTC on 29 December 2015 and 00:00 UTC on 28 January 2016 using the MetPy library in Python.

2.6 ERA5

ERA5 is the fifth generation of the European Centre for Medium-Range Weather Forecasts (ECMWF) reanalysis series (Hersbach et al., 2020). The data are available at a regular horizontal grid spacing of 0.25° and at 137 vertical levels, with hourly resolution. This study utilises ERA5 surface variables, including mean sea level pressure (MSLP), 10-m zonal and meridional wind components (u and v), 2-m air temperature, and relative humidity. Pressure-level variables used in this study include temperature, relative humidity, u and v, specific humidity, and vertical velocity. The dataset used spans from January 2015 to December 2023 with a time resolution of 1 hour. The ERA5 data were used to calculate horizontal moisture convergence as

$$MC = -\nabla_h \cdot (q\mathbf{V}) = -\left[\frac{\partial(qu)}{\partial x} + \frac{\partial(qv)}{\partial y}\right] \tag{2}$$

where ∇_h is the horizontal gradient operator, q is the specific humidity ($\mathrm{kg\,kg^{-1}}$), and $\mathbf{V} = (u, v)$ is the horizontal wind vector.

3 Results

3.1 Weather regime characteristics at DDU

Identification: To identify key weather regimes at DDU, we applied K-means clustering (Hartigan and Wong, 1979) to hourly ERA5 variables (Table 1) for the period 2015–2023, following the methodology and variable selection of Lang et al. (2018). The optimal number of clusters was assessed by analysing solutions ranging from 3 to 8. The elbow method (Thorndike, 1953; Everitt et al., 2011) suggested four clusters. However, the four-cluster configuration produced a strongly imbalanced partitioning, with one regime representing conditions between two weak low-pressure systems (not shown)—accounting for more than 50% of winter occurrences, indicating that several winter circulation states were grouped into a single regime. Increasing the number of clusters to five resolved this issue by separating an additional, physically interpretable regime characterised by a coastal trough or an elongated low-pressure structure along the Antarctic coast. Further increasing the number of clusters

https://doi.org/10.5194/egusphere-2026-4159
Preprint. Discussion started: 13 August 2026

(>5) mainly subdivides existing regimes without introducing new physically distinct circulation patterns. The weather regimes identified at DDU reflect the interaction between Southern Ocean low-pressure systems, Antarctic continental high-pressure systems and coastal boundary-layer processes, which strongly modulate temperature, moisture, and cloud structure over East Antarctica (Parish and Cassano, 2003; Vignon et al., 2019). The weather regimes are described in detail below.

Summer-Warm Air Advection (S-WAA): The S-WAA regime occurs 18% of the time at DDU and is associated with a low-pressure system approaching from the west (Fig. 1a). Humidity is relatively high, especially within the 800–900 hPa layer highlighting the frequent presence of low-level clouds (Fig. 1b). The wind profile is characterised by a weak easterly flow from the surface to 800 hPa, veering to a northeasterly flow at 700 hPa. The winds veer toward a more northwesterly flow at higher altitudes, which serves as an important metric for warm-air intrusions into coastal Antarctica (Silva and Schlosser, 2021). The S-WAA regime shows a strong seasonal cycle, with a peak from November to February (Fig. 1c).

Summer-Dry (S-Dry): The S-Dry regime is the most prevalent at DDU, accounting for 26.5% of the time and peaking between December and February. The composite MSLP shows that DDU lies between two weak low-pressure systems (Fig. 1d), with a southward extension of the subtropical high (50–60°S), resulting in a lower horizontal pressure gradient between the Antarctic continent and the Southern Ocean. The thermodynamic profile indicates a dry troposphere, with the largest dew point depression near 900 hPa (Fig. 1e). Consistently, the lower atmosphere is characterised by weak, dry southerly flow from the Antarctic interior, transitioning to westerly flow aloft.

Winter-Trough (W-Trough): The W-Trough regime occurs about 20% of the time, with the highest frequency in June and July. The MSLP composite shows a weak, elongated low-pressure system extending from 120° to 160°E (Fig. 1g). Winds are southeasterly from the surface to about 800 hP and between 800 and 700 hPa, they weaken before transitioning to westerlies aloft. The thermodynamic profile shows the maximum dew point depression near 900 hPa, decreasing to about 5°C near 800 hPa and remaining relatively humid toward the upper levels of the profile (Fig. 1h).

Winter-Dry (W-Dry): The W-Dry regime occurs 20.5% of the time, with a peak between June and September (Fig. 1l). Although W-Dry regimes' circulation resembles that of the S-Dry regime, it is characterised by southerly flow extending through deeper layers of the troposphere. The MSLP pattern further shows a strengthened continental high (Fig. 1j), likely associated with reduced solar insolation over the Antarctic interior. The dew point depression remains high throughout the troposphere (Fig. 1k) with multiple temperature inversions above 900 hPa.

Low-Pressure (Low-P): The Low-P regime occurs 16% of the time and is characterised by a strong cyclonic circulation north of DDU together with enhanced high pressure over the Antarctic continent (Fig. 1m). The resulting pressure gradient drives an intense, dry southeasterly flow from the Antarctic interior at the lower levels of the atmosphere. With height, the continental flow weakens and veers to easterly, producing a moisture inversion between 900 and 800 hPa (Fig. 1n). Similar vertical moisture structures have been observed during cyclonically forced offshore flow events at Neumayer Station in coastal Dronning Maud Land, East Antarctica (Silva and Schlosser, 2021). Unlike other weather regimes, Low-P shows little seasonal variability (Fig. 1o) and represents year-round cyclone influence associated with the Southern Ocean storm track.

https://doi.org/10.5194/egusphere-2026-4159
Preprint. Discussion started: 13 August 2026

3.1.1 Observed and ERA5 precipitation for synoptic regimes:

Pluvo[2] observations show an accumulated precipitation of 5027.0 mm at DDU between 17 November 2015 and 30 April 2023 (Table 2). For the same period, considering only hours with available precipitation observations, ERA5 estimates a total precipitation of 3684.0 mm and shows a correlation coefficient of 0.45 ($p < 0.05$). Wiener et al. (2024) estimated an MRR-derived mean annual snowfall accumulation of 1060 $\mathrm{mm\,yr^{-1}}$ at 300 m above the DDU station over a nearly comparable period. The surface accumulation derived in our study is 32.5% lower than this estimate, consistent with the nearly 35% snowfall loss attributed to katabatic-wind-driven sublimation along the margins of East Antarctica by Grazioli et al. (2017b). The S-WAA regime produces the highest surface precipitation at DDU, with a total accumulation of 2408 mm, accounting for 49% of the total precipitation with a mean rate of 0.21 $\mathrm{mm\,h^{-1}}$. For this regime, ERA5 estimates a total accumulation of 2289 mm, corresponding to a mean precipitation rate of 0.20 $\mathrm{mm\,h^{-1}}$ (Table 2). Nevertheless, ERA5 precipitation during S-WAA shows a solid agreement with observations, with a correlation coefficient of 0.56 ($p<0.05$). Low-P is the second-largest contributor to total precipitation at DDU, where the total observed (ERA5) precipitation accumulation is 2328 (1206) mm. The observed and ERA5 precipitation in this regime are associated with a correlation coefficient of 0.37 ($p<0.05$). Notably, S-WAA and Low-P together account for 94.2% of the total observed precipitation at DDU, indicating that these two synoptic regimes dominate the station's precipitation climatology. The W-Trough shows a lower observed surface precipitation rate (0.02 $\mathrm{mm\,h^{-1}}$). The S-Dry and W-Dry regimes do not produce measurable precipitation at DDU, which is dominated by continental air masses advected from the Antarctic interior.

3.2 Microphysics of cloud hydrometeor growth in Low-P and S-WAA regimes: case studies

We now analyse two case studies, one during the Low-P (29 December 2015) and the other in the S-WAA weather regime (28 January 2016) (Fig. 2). These cases were selected based on the presence of a strong precipitation core aloft, which coincides with the availability of all co-located multi-platform observations from the APRES3 campaign.

3.2.1 Low-P Case study

The Low-P regime event started at 16:00 UTC on 28 December 2015. It persisted for 32 hours until 00:00 UTC on 30 December 2015, during which an extended and intense low-pressure area spanned a broad longitudinal sector from 110°E to 160°E (Fig. 2a). Along the coastal ocean within this longitude range, the MSLP ranges from 975 to 988 hPa, while over the Antarctic continental interior, high-pressure conditions occur at 1000–1010 hPa. Here, the X-band radar VAD profiles and radiosonde winds show strong continental southeasterly flow in the lower troposphere, extending up to an altitude of 1 km (Fig. 3a, d). Consistently, an intense downslope wind below 1 km is produced in the ERA5-based analysis (Fig. 4b). The downslope flow leads to the drying of the lower atmosphere, resulting in a large dew point depression of 10°C at the surface level (Fig. 3c).

Evolution of the precipitation column: Initially, Z_e remains weak throughout the column, indicating limited hydrometeor growth and a small precipitation mass flux (Fig. 5a). As the system matures, observations show an intense precipitation core at DDU from 00:00 UTC (29 December), accompanied by a Z_e maximum confined between the altitudes of 1 and 3 km.

https://doi.org/10.5194/egusphere-2026-4159
Preprint. Discussion started: 13 August 2026

This Z_e intensification coincides with increases in surface precipitation (Fig. 5e) with an episodic pattern during this period. After 03:00 UTC, the Z_e core weakens and becomes shallower (mainly between 1 and 2 km). The quartiles (25%, 75%) and the Median of Z_e show a pronounced decrease towards the surface from $1\,\mathrm{km}$ (Fig. 5c), indicating a substantial reduction in hydrometeor mass.

Radar signatures of hydrometeor characteristics and growth: To examine precipitation growth mechanisms, the polarimetric radar variables Z_{H}, Z_{DR}, K_{DP}, and ρ_{HV} are analysed from 00:00 to 03:00 UTC on 28 December 2015 (Fig. 5a; two vertical black lines denote the analysed precipitation column). To understand the temporal evolution of microphysical processes, the polarimetric variables were averaged over 15-min intervals using quality-controlled measurements from RHI scans at elevations between 0° and 40° and grouped into 100-m vertical bins (Fig. 6a–d). Owing to the scanning geometry, the measurements contributing to each profile were obtained over a range of horizontal distances from the radar, with a median distance of approximately 8.7 km. The polarimetric profiles in Fig. 6, mainly Z_{H} and K_{DP}, reveal a contrasting pattern for the Low-P case between 00:00–01:30 UTC and 01:30–03:00 UTC. Thus, these two periods are examined separately in detail.

Early phase of cloud growth (00:00–01:30 UTC): Fig 6 (a-d) shows increasing Z_{H}, K_{DP}, and ρ_{HV} and decreasing Z_{DR} toward the surface within the DGZ temperature range -10 to -14°C (2–3.5 km). These polarimetric observations are consistent with hydrometeor growth via riming and increased concentrations of small ice crystals (Kumjian et al., 2022). The interpretation of the riming initiation in DGZ is corroborated by enhanced moisture convergence (Fig. 4a), which likely increases the occurrence of supercooled liquid water and favours riming. A recent study by Kötsche et al. (2025) noted that at temperatures between -15 and -10°C, the maximum spectral Z_{DR} decreases, while Z_e and K_{DP} increase. They pointed out that this signature might indicate the early-stage formation of D-type aggregates (D-type particles include pristine dendrites, plates, and needles, which generally have relatively high densities and strongly anisotropic shapes (Schrom and Kumjian, 2016; Griffin et al., 2018). If supercooled liquid water were available in this layer, the dendrites could also become rimmed, forming even graupel (Grazioli et al., 2015). Earlier studies have shown that secondary ice production (SIP) can enhance K_{DP} (Andrić et al., 2013; Sinclair et al., 2016), as K_{DP} is particularly sensitive to the concentration of small, anisotropic ice particles and is less affected by larger hydrometeors that dominate radar reflectivity. So, the enhanced K_{DP} observed in this DGZ may indicate higher concentrations of small ice crystals associated with ice-ice collisions and possible SIP (Fig. 6c). Furthermore, rimed particles coexisting with unrimed ice may likely increase collision efficiency. These observations emphasise that SIP may occur at temperatures below -8°C, extending beyond the temperature range typically represented in many numerical weather models. Although the SIP can increase K_{DP}, the Doppler spectrogram (Fig. 7a) do not exhibit a distinct multimodal spectral reflectivity distribution, which is indicative of distinct hydrometeor populations within the radar sampling volume and can be used to infer SIP (Luke and Kollias, 2013). The absence of such a signature does not necessarily preclude SIP, as instrument sampling volumes differ between spectrogram and polarimetric signatures. Consequently, Doppler spectral observations do not provide direct evidence of SIP, whereas polarimetric signatures suggest the possible occurrence of SIP within the DGZ. Below the DGZ, down to 1 km altitude, the Z_{H} profiles mostly increase to 22 dBZ, while Z_{DR} and K_{DP} decrease to about 0.5 dB and $0.025°\,\mathrm{km}^{-1}$, respectively. The increase in Z_{H}, together with the reduction in Z_{DR} and K_{DP}, suggests the presence of larger, more isotropic hydrometeors and a decrease in the concentration of small anisotropic ice particles. Such polarimetric

https://doi.org/10.5194/egusphere-2026-4159
Preprint. Discussion started: 13 August 2026

patterns imply a riming-driven growth process and when hydrometeor anisotropies are weak, aggregation can produce similar polarimetric signatures (Kumjian et al., 2022). The temperature range within the altitudes is from -10 to -7 °C, where the Doppler velocity steadily increases from 1 $\mathrm{m\,s^{-1}}$ to about 1.25 $\mathrm{m\,s^{-1}}$ (Fig. 8a), indicating the continuous growth of hydrometeors possibly by riming. Alexander et al. (2023) showed that riming frequency increases inside the clouds at temperatures warmer than -10 °C during the Antarctic summer. Considering the fall velocities in the layer below 1km, they frequently exceed 1.5 $\mathrm{m\,s^{-1}}$ (Fig. 8a). Given that rimed particles generally have a fall speed of 1.5–2.5 $\mathrm{m\,s^{-1}}$ or higher (Mosimann, 1995; Barthazy and Schefold, 2006), the observed fall speed in the Low-P case suggests that the particles reaching the surface are largely rimed. At the same time, Z_{H} shows a sharp decrease, and Z_{DR} remains relatively constant below 1 km (Fig. 6a-c), consistent with hydrometeor mass loss due to sublimation (Carlin et al., 2021; Grazioli et al., 2017b). K_{DP} profile displays an increasing pattern within this layer (Fig. 6c), probably indicating sublimation-induced fragmentation-a plausible mechanism for SIP (Oraltay and Hallett, 1989; Korolev and Leisner, 2020). The temperature at this altitude ranges from -3 to -7 °C and overlaps the Hallett–Mossop zone (HM) (Hallett and Mossop, 1974), where SIPs occur primarily via droplet freezing and shattering. However, the negligible moisture content at these altitudes below 1km, and thus the limited availability of supercooled liquid water, makes an active HM process very unlikely to occur here. The Doppler spectrograms together with spectral width from MRR reveal pronounced spectral broadening (Figs. 7a and 8b), which would imply wind-driven turbulence in this layer (Garrett and Yuter, 2014).

Later phase of cloud growth (01:30–03:00 UTC): Z_{H} weakens toward the surface over this period with a significant drop below 2 km altitude (Fig. 6a). The K_{DP} values are considerably lower throughout the column, suggesting a lower concentration of small anisotropic ice crystals, possibly due to reduced hydrometeor collisions and sublimation-induced fragmentation. The overall fall-velocity structure remains broadly similar to that observed earlier in the event; however, a marked decrease in fall velocity is evident between approximately 1.5 and 1 km altitude (Fig. 8a). Below 1 km, spectral broadening becomes less pronounced (Fig. 8b) likley due to the weaker wind speed during this phase (Fig. S1) and associated reduction in the turbulence.

Surface Hydrometeor Observations: The MASC-based analysis during the Low-P case shows a predominance of graupel at the surface and provides direct evidence of efficient riming within the cloud layer (Fig. 7b). However, aggregates and planar crystals are largely absent. Therefore, the observations from the polarimetric radar, MRR, and MASC indicate that hydrometeor growth is likely driven by riming processes aloft during the Low-P case, with graupel efficiently reaching the surface.

3.2.2 S-WAA case study

The S-WAA case study spans from 00:00 UTC on 28 January 2016 to 12:00 UTC on 29 January 2016 (Fig. 2c, d). During the S-WAA case, the mean MSLP at DDU reached a minimum of 977 hPa, and the mean 2-m air temperature fell below $-3.0\,°\mathrm{C}$ (Fig. 2c, d). The low associated with the S-WAA regime is partially blocked by a ridge located northeast of DDU over the Southern Ocean, which may limit its eastward propagation. The radar and radiosonde winds during this S-WAA case display a weak easterly flow near the surface, with reduced influence of dry continental air (Fig. 3b, e). From 500 m upward, the flow strengthens and gradually veers northeasterly above 1 km, resulting in strong moisture convergence extending from 500

https://doi.org/10.5194/egusphere-2026-4159
Preprint. Discussion started: 13 August 2026

m to 1.5 km altitude (Figs. 3b and 4a). Enhanced boundary-layer moisture content and vertically coherent ascent with weak downslope flow during the S-WAA (Fig. 4a, c), facilitating efficient precipitation at the surface (Fig. 5f).

Evolution of the precipitation column: MRR observations show that the Z_e maxima extends towards the 300m altitudes during the S-WAA event (Fig. 5b). Further, the Z_e across the 25$^{\mathrm{th}}$, median, and 75$^{\mathrm{th}}$ percentiles consistently increases toward the surface, indicating systematic growth and/or increasing concentration of hydrometeors (Fig. 5d). The enhanced Z_e at lower altitudes is associated with persistent surface precipitation, with hourly rates exceeding $1\,\mathrm{mm\,h^{-1}}$ for several hours. ERA5 closely represents the observed surface precipitation during the S-WAA case, with a similar peak followed by a steady drop (Figs. 2d and 5f). After 06:00 UTC, the Z_e core weakened and was confined mainly to an altitude range of 300-600 m. A secondary intensification of the Z_e occurs after approximately 11:25 UTC, during which the Z_e core deepens again to an altitude of 2 km (Fig. 5b).

Radar signatures of hydrometeor characteristics and growth: We now examine the S-WAA case between 00:00 and 03:00 UTC on 28 January 2016 (Fig. 5b; two vertical black lines denote the analysed precipitation column).

Early phase of cloud growth (00:00–01:00 UTC): Here, the DGZ extends from 1.5 to 3.5 km. In the upper half of the DGZ (2.5 to 3.5km, -14 to -20 °C), an increase in Z_{H} towards the surface and a high Z_{DR} with minimal variability is observed (Fig. 6e, f). Such changes are consistent with vapour-depositional growth that increases particle size without significant changes in crystal shape (Oue et al., 2016; Schrom et al., 2021). Previous studies have shown that depositional growth rates maximise near -15 °C, favouring the formation of dendritic ice crystals (Rogers and Yau). Within the lower half of the DGZ, Z_{H} and ρ_{HV} continue to increase toward the surface, accompanied by a marked reduction in Z_{DR} from 1.25 to 0.5 dB. The polarimetric signatures, together with a fall speed below 1 $\mathrm{m\,s^{-1}}$ (Fig. 8c), indicate an increasing influence of aggregation on hydrometeor growth in this layer. Earlier studies have shown that aggregation is associated with higher Z_{H}, lower Z_{DR}, and increased ρ_{HV} (Vogel and Fabry, 2018). The Z_{H} increases from 10 dBZ to 25 dBZ (Fig. 6e) with time between 0.5 and 1.5 km (-10 to -6°C), representing the evolution of hydrometeor size and number concentration. However, they largely retain their original shape, as indicated by the nearly constant Z_{DR} in most profiles (Fig. 6f). In this altitude range of 0.5 to 1.5 km, we observed an increasing fall speed (>1.5 $\mathrm{m\,s^{-1}}$) and an enhanced moisture convergence, hence supporting hydrometeor growth by riming (Figs. 4a, 7c, and 8c). Furthermore, this cloud layer is characterised by enhanced K_{DP} values (Fig. 6g) and a bimodal Doppler velocity distribution (Fig. 7c), providing strong evidence of secondary ice production, more likely resulting from the HM process (Hallett and Mossop, 1974).

Later phase of cloud growth (01:00–03:00 UTC): As in the first phase, the polarimetric signatures in the upper half of the DGZ (2.5–3.5 km) indicate vapour-depositional growth. In the lower half of it, Z_{H} increases, while Z_{DR} decreases more gradually toward the surface than in the earlier phase (Fig. 6e, f). At the same time, K_{DP} exhibits a pronounced increase within this layer compared with the first phase (Fig. 6g), with most profiles exceeding 0.1$^{\circ}\,\mathrm{km^{-1}}$ and reaching nearly 0.2$^{\circ}\,\mathrm{km^{-1}}$ at 02:15 UTC. The strong SIP may contribute to the increase in K_{DP}, possibly through the collisional breakup of aggregates within the layer (Vardiman, 1978; Takahashi and Nagao, 1995; Sotiropoulou et al., 2021). Fig. 8c represents the decrease in Doppler velocity towards the surface within the DGZ. For instance, the Doppler velocity decreases from 1.25 $\mathrm{m\,s^{-1}}$ at 3.5 km (02:15 UTC) to 0.75 $\mathrm{m\,s^{-1}}$ at 1.5 km. The combined evolution of the K_{DP} and Doppler velocity profiles suggests that enhancement

https://doi.org/10.5194/egusphere-2026-4159
Preprint. Discussion started: 13 August 2026

of small, slowly falling ice particles via SIP shifts the mean Doppler velocity toward lower values than in the initial phase. The 1.0–2.0 km cloud layer exhibits an increasing Z_{H}, decreasing Z_{DR} with Doppler velocities dropping to approximately 0.5 $\mathrm{m\,s^{-1}}$ (Figs. 6e-f and 8c). These signatures indicate larger, less-dense hydrometeors and imply an aggregation-driven process in this phase (Kumjian et al., 2022). While below 1 km, Z_{H} remains close to 20 dBZ, and K_{DP} remains elevated (>0.1°, km^{-1}), while Doppler velocities increase towards the surface, reaching nearly 1 $\mathrm{m\,s^{-1}}$. We interpret riming and SIP to persist below 1 km and continue to play a leading role in hydrometeor growth.

Surface Hydrometeor Observations: MASC observations show a relatively high and comparable occurrence of aggregates and graupel (Fig. 7d), consistent with aggregation and riming processes inferred from the radar data. Further, the occurrence of columnar and planar crystals provides more conclusive evidence of vapour-depositional growth (Hashino and Tripoli, 2007). Thus, the polarimetric radar, MRR, and MASC observations collectively indicate vapour deposition within the DGZ, followed by aggregation and riming at lower levels, with the HM process contributing to secondary ice production.

4 Summary and conclusions

We identified five distinct weather regimes over DDU using K-means clustering. Of these weather regimes, the S-WAA and Low-P account for 94.2% of the observed surface precipitation, occurring 34% of the time collectively. The W-Trough regime contributes 5.0% of total precipitation, whereas the S-Dry and W-Dry regimes represent extremely dry tropospheric conditions under dominant continental flow from the Antarctic interior. Observed surface precipitation is moderately correlated with ERA5 precipitation overall ($r = 0.45$, $p < 0.05$), as well as during the S-WAA ($r = 0.56$, $p < 0.05$) and Low-P ($r = 0.37$, $p < 0.05$) regimes on an hourly timescale, emphasising that ERA5 moderately captures precipitation variability associated with the important precipitation-bearing weather patterns.

Representative Low-P (29 December 2015) and S-WAA (28 January 2016) events were examined in detail to investigate the microphysical evolution of precipitation. The Low-P event is characterised by strong downslope flow that results in boundary-layer drying, leading to intermittent surface precipitation despite a well-developed precipitation column aloft. The results are consistent with previous studies showing that katabatic-flow-driven sublimation can reduce surface precipitation along the Antarctic coast (Tomikawa et al., 2015; Alexander et al., 2017; Grazioli et al., 2017b). As these processes occur within the near-surface satellite blind zone, they may be poorly represented in satellite snowfall estimates, and our results therefore highlight the importance of validating satellite-derived precipitation with ground-based observations in high-latitude regions (Stephens et al., 2002; Maahn et al., 2014; Skofronick-Jackson et al., 2017). The analysis of polarimetric signatures during this Low-P case study indicates riming within the DGZ (2-3.5 km, -10 to -14 °C). Riming intensifies between 1 and 2 km (-7 to -10 °C), accompanied by an increase in the concentration of small ice crystals, likely due to SIP within this cloud layer (Fig. 9a). These observations agree with previous studies showing that riming becomes more likely at temperatures warmer than approximately -12 °C due to the increased availability of supercooled liquid water (Kneifel and Moisseev, 2020). The layer below 1 km is characterised by significant sublimation-driven hydrometeor mass loss and SIP associated with sublimation-induced fragmentation. MASC observations showing a predominance of graupel at the surface further underscore the riming-

https://doi.org/10.5194/egusphere-2026-4159
Preprint. Discussion started: 13 August 2026

driven growth of hydrometeors during this event. The S-WAA case features a relatively moist lower troposphere driven by oceanic flow, thereby enabling efficient transport of hydrometeors to the surface and leading to persistent precipitation. The hydrometeor growth is characterised by vapour deposition in the upper half of the DGZ (2.5-3.5 km, -14 to -20 °C) and aggregation in the lower half (1.5-2.5 km, -10 to -14 °C) (Fig. 9b), where increased concentrations of small ice crystals are likely associated with collisional breakup. Efficient riming is observed below 1km (above -8 °C), with a SIP signature that possibly indicates the HM process. Surface observations during this S-WAA event reveal comparable contributions from graupel and aggregates, as well as columnar and planar crystals, consistent with the coexistence of multiple hydrometeor growth processes and SIP.

Changes in ice crystal number concentration through SIP can substantially modify cloud radiative effects, which in turn can influence ice-shelf surface melting (Gilbert et al., 2020), highlighting the broader importance of accurately representing cloud microphysical processes in Antarctic models. In this context, our findings provide observational evidence that hydrometeor growth and surface precipitation over coastal East Antarctica can vary substantially between weather regimes. Our hydrometeor growth analysis was limited to selected S-WAA and Low-P cases for which all relevant instrumental observations were available to characterise their microphysical features. Therefore, while these cases reveal distinct regime-dependent microphysical pathways, the observed radar signatures cannot yet be considered representative of all events within these regimes. Moreover, interactions among synoptic forcing, local flow including katabatic winds, and microphysical growth are likely to vary along the Antarctic coast because of regional differences in orography and exposure to maritime air masses. Future research extending the analysis to a larger number of events and additional Antarctic coastal sites could determine how frequently these microphysical signatures occur within each regime and assess the role of regional orography in modulating cloud and precipitation processes. Such efforts will help refine the representation of precipitation formation in weather and climate models.

Code availability. Codes are available upon reasonable request to the corresponding author.

Data availability. The APRES3 MRR, Pluvio^2, and MASC data used in this study are available from PANGAEA at https://doi.pangaea.de/10.1594/PANGAEA.883562 (Grazioli et al., 2017a) and https://doi.pangaea.de/10.1594/PANGAEA.962727 (Wiener et al., 2024). The MXPol data used in this study are available upon request from Alexis Berne. ERA5 data are available from the Copernicus Climate Data Store at https://cds.climate.copernicus.eu.

Author contributions. S.A.V., P.M., A.B. and S.S. designed the study. S.A.V. performed the analysis and wrote the initial manuscript. S.S., P.M., H.C., and A.B. contributed to constructive discussions of the results and provided valuable ideas and feedback. All authors contributed to the final version of the manuscript.

https://doi.org/10.5194/egusphere-2026-4159
Preprint. Discussion started: 13 August 2026

Competing interests. The authors declare that they have no known competing financial interests or personal relationships that could have influenced the work reported in this paper.

Acknowledgements. This research has been supported by the Australian Research Council's Securing Antarctica's Environmental Future (SAEF) Project (SR200100005). We would like to thank all the researchers involved in the APRES3 campaign for their contributions to data collection, instrument operation, quality control, data processing, and campaign coordination, which made this study possible.

Financial support. This work was supported by ARC SRIEAS Grant SR200100005 Securing Antarctica's Environmental Future.

https://doi.org/10.5194/egusphere-2026-4159
Preprint. Discussion started: 13 August 2026

References

Alexander, S., Orr, A., Webster, S., and Murphy, D.: Observations and fine-scale model simulations of gravity waves over Davis, East Antarctica (69° S, 78° E), Journal of Geophysical Research: Atmospheres, 122, 7355–7370, 2017.

Alexander, S., Protat, A., Berne, A., and Ackermann, L.: Radar-derived snowfall microphysical properties at Davis, Antarctica, Journal of Geophysical Research: Atmospheres, 128, e2022JD038 389, 2023.

Andrić, J., Kumjian, M. R., Zrnić, D. S., Straka, J. M., and Melnikov, V. M.: Polarimetric signatures above the melting layer in winter storms: An observational and modeling study, Journal of Applied Meteorology and Climatology, 52, 682–700, 2013.

Barthazy, E. and Schefold, R.: Fall velocity of snowflakes of different riming degree and crystal types, Atmospheric research, 82, 391–398, 2006.

Bodart, J. and Bingham, R.: The impact of the extreme 2015–2016 El Niño on the mass balance of the Antarctic ice sheet, Geophysical Research Letters, 46, 13 862–13 871, 2019.

Bodas-Salcedo, A., Andrews, T., Karmalkar, A., and Ringer, M.: Cloud liquid water path and radiative feedbacks over the Southern Ocean, Geophysical Research Letters, 43, 10–938, 2016.

Boening, C., Lebsock, M., Landerer, F., and Stephens, G.: Snowfall-driven mass change on the East Antarctic ice sheet, Geophysical Research Letters, 39, 2012.

Browning, K. and Wexler, R.: The determination of kinematic properties of a wind field using Doppler radar, Journal of Applied meteorology and climatology, 7, 105–113, 1968.

Carlin, J. T., Reeves, H. D., and Ryzhkov, A. V.: Polarimetric observations and simulations of sublimating snow: Implications for nowcasting, Journal of Applied Meteorology and Climatology, 60, 1035–1054, 2021.

Connolly, P., Emersic, C., and Field, P.: A laboratory investigation into the aggregation efficiency of small ice crystals, Atmospheric Chemistry and Physics, 12, 2055–2076, 2012.

Dalaiden, Q., Goosse, H., Lenaerts, J. T., Cavitte, M. G., and Henderson, N.: Future Antarctic snow accumulation trend is dominated by atmospheric synoptic-scale events, Communications Earth & Environment, 1, 62, 2020.

Dale, E. R., McDonald, A. J., Coggins, J. H., and Rack, W.: Atmospheric forcing of sea ice anomalies in the Ross Sea polynya region, The Cryosphere Discussions, 2016, 1–21, 2016.

Dedekind, Z., Grazioli, J., Austin, P. H., and Lohmann, U.: Heavy snowfall event over the Swiss Alps: did wind shear impact secondary ice production?, Atmospheric Chemistry and Physics, 23, 2345–2364, 2023.

DeLaFrance, A., McMurdie, L. A., Rowe, A. K., and Conrick, R.: Effects of riming on ice-phase precipitation growth and transport over an orographic barrier, Journal of Advances in Modeling Earth Systems, 16, e2023MS003 778, 2024.

Di Natale, G., Turner, D. D., Bianchini, G., Del Guasta, M., Palchetti, L., Bracci, A., Baldini, L., Maestri, T., Cossich, W., Martinazzo, M., et al.: Consistency test of precipitating ice cloud retrieval properties obtained from the observations of different instruments operating at Dome C (Antarctica), Atmospheric Measurement Techniques, 15, 7235–7258, 2022.

Durán-Alarcón, C., Boudevillain, B., Genthon, C., Grazioli, J., Souverijns, N., van Lipzig, N. P., Gorodetskaya, I. V., and Berne, A.: The vertical structure of precipitation at two stations in East Antarctica derived from micro rain radars, The Cryosphere, 13, 247–264, 2019.

Everitt, B. S., Landau, S., Leese, M., and Stahl, D.: Cluster analysis, 2011.

Ferrone, A. and Berne, A.: Radar and ground-level measurements of clouds and precipitation collected during the POPE 2020 campaign at Princess Elisabeth Antarctica, Earth System Science Data, 15, 1115–1132, 2023.

Field, P. R., Lawson, R. P., Brown, P. R., Lloyd, G., Westbrook, C., Moisseev, D., Miltenberger, A., Nenes, A., Blyth, A., Choularton, T., et al.: Secondary ice production: Current state of the science and recommendations for the future, Meteorological Monographs, 58, 7–1, 2017.

Garrett, T., Fallgatter, C., Shkurko, K., and Howlett, D.: Fall speed measurement and high-resolution multi-angle photography of hydrometeors in free fall, Atmospheric Measurement Techniques, 5, 2625–2633, 2012.

Garrett, T. J. and Yuter, S. E.: Observed influence of riming, temperature, and turbulence on the fallspeed of solid precipitation, Geophysical Research Letters, 41, 6515–6522, 2014.

Gehring, J., Vignon, É., Billault-Roux, A.-C., Ferrone, A., Protat, A., Alexander, S. P., and Berne, A.: Orographic flow influence on precipitation during an atmospheric river event at Davis, Antarctica, Journal of Geophysical Research: Atmospheres, 127, e2021JD035 210, 2022.

Genthon, C., Berne, A., Grazioli, J., Durán Alarcón, C., Praz, C., and Boudevillain, B.: Precipitation at Dumont d'Urville, Adélie Land, East Antarctica: the APRES3 field campaigns dataset, Earth System Science Data, 10, 1605–1612, 2018.

Gilbert, E., Orr, A., King, J. C., Renfrew, I., Lachlan-Cope, T., Field, P., and Boutle, I.: Summertime cloud phase strongly influences surface melting on the Larsen C ice shelf, Antarctica, Quarterly Journal of the Royal Meteorological Society, 146, 1575–1589, 2020.

Grazioli, J., Lloyd, G., Panziera, L., Hoyle, C. R., Connolly, P. J., Henneberger, J., and Berne, A.: Polarimetric radar and in situ observations of riming and snowfall microphysics during CLACE 2014, Atmospheric Chemistry and Physics, 15, 13 787–13 802, 2015.

Grazioli, J., Genthon, C., Boudevillain, B., Duran-Alarcon, C., Del Guasta, M., Madeleine, J.-B., and Berne, A.: Measurements of precipitation in Dumont d'Urville, Adélie Land, East Antarctica, The Cryosphere, 11, 1797–1811, 2017a.

Grazioli, J., Madeleine, J.-B., Gallée, H., Forbes, R. M., Genthon, C., Krinner, G., and Berne, A.: Katabatic winds diminish precipitation contribution to the Antarctic ice mass balance, Proceedings of the National Academy of Sciences, 114, 10 858–10 863, 2017b.

Grazioli, J., Ghiggi, G., Billault-Roux, A.-C., and Berne, A.: MASCDB, a database of images, descriptors and microphysical properties of individual snowflakes in free fall, Scientific data, 9, 186, 2022.

Griffin, E. M., Schuur, T. J., and Ryzhkov, A. V.: A polarimetric analysis of ice microphysical processes in snow, using quasi-vertical profiles, Journal of Applied Meteorology and Climatology, 57, 31–50, 2018.

Hallett, J. and Mossop, S.: Production of secondary ice particles during the riming process, Nature, 249, 26–28, 1974.

Hansen, J., Sato, M., Hearty, P., Ruedy, R., Kelley, M., Masson-Delmotte, V., Russell, G., Tselioudis, G., Cao, J., Rignot, E., et al.: Ice melt, sea level rise and superstorms: evidence from paleoclimate data, climate modeling, and modern observations that 2$\circ$ C global warming could be dangerous, Atmospheric Chemistry and Physics, 16, 3761–3812, 2016.

Hartigan, J. A. and Wong, M. A.: Algorithm AS 136: A k-means clustering algorithm, Journal of the royal statistical society. series c (applied statistics), 28, 100–108, 1979.

Hashino, T. and Tripoli, G.: The Spectral Ice Habit Prediction System (SHIPS). Part I: Model description and simulation of the vapor deposition process, Journal of the Atmospheric Sciences, 64, 2210–2237, 2007.

Hersbach, H., Bell, B., Berrisford, P., Hirahara, S., Horányi, A., Muñoz-Sabater, J., Nicolas, J., Peubey, C., Radu, R., Schepers, D., et al.: The ERA5 global reanalysis, Quarterly journal of the royal meteorological society, 146, 1999–2049, 2020.

Heymsfield, A. J., Schmitt, C., Chen, C.-C.-J., Bansemer, A., Gettelman, A., Field, P. R., and Liu, C.: Contributions of the liquid and ice phases to global surface precipitation: Observations and global climate modeling, Journal of the Atmospheric Sciences, 77, 2629–2648, 2020.

https://doi.org/10.5194/egusphere-2026-4159
Preprint. Discussion started: 13 August 2026

Hofer, S., Amory, C., Kittel, C., Carlsen, T., Le Toumelin, L., and Storelvmo, T.: The contribution of drifting snow to cloud properties and the atmospheric radiative budget over Antarctica, Geophysical Research Letters, 48, e2021GL094 967, 2021.

Holleman, I.: Quality control and verification of weather radar wind profiles, Journal of Atmospheric and Oceanic Technology, 22, 1541–1550, 2005.

Kim, B.-H., Seo, K.-W., Eom, J., Chen, J., and Wilson, C. R.: Antarctic ice mass variations from 1979 to 2017 driven by anomalous precipitation accumulation, Scientific reports, 10, 20 366, 2020.

Kneifel, S. and Moisseev, D.: Long-term statistics of riming in nonconvective clouds derived from ground-based Doppler cloud radar observations, Journal of the Atmospheric Sciences, 77, 3495–3508, 2020.

Korolev, A. and Leisner, T.: Review of experimental studies of secondary ice production, Atmospheric Chemistry and Physics, 20, 11 767–11 797, 2020.

Kötsche, A., Myagkov, A., Von Terzi, L., Maahn, M., Ettrichrätz, V., Vogl, T., Ryzhkov, A., Bukovcic, P., Ori, D., and Kalesse-Los, H.: Investigating KDP signatures inside and below the dendritic growth layer with W-band Doppler radar and in situ snowfall camera, Atmospheric Chemistry and Physics, 25, 14 045–14 070, 2025.

Kumjian, M. R.: Principles and applications of dual-polarization weather radar. Part I: Description of the polarimetric radar variables, J. Oper. Meteor, 1, 226–242, 2013.

Kumjian, M. R., Mishra, S., Giangrande, S. E., Toto, T., Ryzhkov, A. V., and Bansemer, A.: Polarimetric radar and aircraft observations of saggy bright bands during MC3E, Journal of Geophysical Research: Atmospheres, 121, 3584–3607, 2016.

Kumjian, M. R., Prat, O. P., Reimel, K. J., van Lier-Walqui, M., and Morrison, H. C.: Dual-polarization radar fingerprints of precipitation physics: A review, Remote Sensing, 14, 3706, 2022.

Lang, F., Huang, Y., Siems, S., and Manton, M.: Characteristics of the marine atmospheric boundary layer over the Southern Ocean in response to the synoptic forcing, Journal of Geophysical Research: Atmospheres, 123, 7799–7820, 2018.

Lawson, R. P. and Gettelman, A.: Impact of Antarctic mixed-phase clouds on climate, Proceedings of the National Academy of Sciences, 111, 18 156–18 161, 2014.

Lemonnier, F., Madeleine, J.-B., Claud, C., Palerme, C., Genthon, C., L'Ecuyer, T., and Wood, N. B.: CloudSat-inferred vertical structure of snowfall over the Antarctic continent, Journal of Geophysical Research: Atmospheres, 125, e2019JD031 399, 2020.

Ligtenberg, S., Van de Berg, W., Van den Broeke, M., Rae, J., and Van Meijgaard, E.: Future surface mass balance of the Antarctic ice sheet and its influence on sea level change, simulated by a regional atmospheric climate model, Climate dynamics, 41, 867–884, 2013.

Listowski, C. and Lachlan-Cope, T.: The microphysics of clouds over the Antarctic Peninsula–Part 2: modelling aspects within Polar WRF, Atmospheric Chemistry and Physics, 17, 10 195–10 221, 2017.

Locatelli, J. D. and Hobbs, P. V.: Fall speeds and masses of solid precipitation particles, Journal of Geophysical Research, 79, 2185–2197, 1974.

Luke, E. P. and Kollias, P.: Separating cloud and drizzle radar moments during precipitation onset using Doppler spectra, Journal of Atmospheric and Oceanic Technology, 30, 1656–1671, 2013.

Maahn, M. and Kollias, P.: Improved Micro Rain Radar snow measurements using Doppler spectra post-processing, Atmospheric Measurement Techniques, 5, 2661–2673, 2012.

Maahn, M., Burgard, C., Crewell, S., Gorodetskaya, I. V., Kneifel, S., Lhermitte, S., Van Tricht, K., and van Lipzig, N. P.: How does the spaceborne radar blind zone affect derived surface snowfall statistics in polar regions?, Journal of Geophysical Research: Atmospheres, 119, 13–604, 2014.

https://doi.org/10.5194/egusphere-2026-4159
Preprint. Discussion started: 13 August 2026

Marshall, G. J., Thompson, D. W., and van den Broeke, M. R.: The signature of Southern Hemisphere atmospheric circulation patterns in Antarctic precipitation, Geophysical Research Letters, 44, 11–580, 2017.

Mathiot, P., Jourdain, N. C., Barnier, B., Gallée, H., Molines, J. M., Le Sommer, J., and Penduff, T.: Sensitivity of coastal polynyas and high-salinity shelf water production in the Ross Sea, Antarctica, to the atmospheric forcing, Ocean Dynamics, 62, 701–723, 2012.

Medley, B. and Thomas, E.: Increased snowfall over the Antarctic Ice Sheet mitigated twentieth-century sea-level rise, Nature Climate Change, 9, 34–39, 2019.

Milani, L., Kulie, M. S., Casella, D., Dietrich, S., L'Ecuyer, T. S., Panegrossi, G., Porcù, F., Sanò, P., and Wood, N. B.: CloudSat snowfall estimates over Antarctica and the Southern Ocean: An assessment of independent retrieval methodologies and multi-year snowfall analysis, Atmospheric research, 213, 121–135, 2018.

Moisseev, D. N., Lautaportti, S., Tyynela, J., and Lim, S.: Dual-polarization radar signatures in snowstorms: Role of snowflake aggregation, Journal of Geophysical Research: Atmospheres, 120, 12 644–12 655, 2015.

Mosimann, L.: An improved method for determining the degree of snow crystal riming by vertical Doppler radar, Atmospheric research, 37, 305–323, 1995.

Oraltay, R. and Hallett, J.: Evaporation and melting of ice crystals: A laboratory study, Atmospheric research, 24, 169–189, 1989.

Oue, M., Galletti, M., Verlinde, J., Ryzhkov, A., and Lu, Y.: Use of X-band differential reflectivity measurements to study shallow Arctic mixed-phase clouds, Journal of Applied Meteorology and Climatology, 55, 403–424, 2016.

Palerme, C., Kay, J., Genthon, C., l'Ecuyer, T., Wood, N., and Claud, C.: How much snow falls on the Antarctic ice sheet?, The Cryosphere, 8, 1577–1587, 2014.

Palerme, C., Genthon, C., Claud, C., Kay, J. E., Wood, N. B., and L'Ecuyer, T.: Evaluation of current and projected Antarctic precipitation in CMIP5 models, Climate dynamics, 48, 225–239, 2017.

Parish, T. R. and Bromwich, D. H.: Reexamination of the near-surface airflow over the Antarctic continent and implications on atmospheric circulations at high southern latitudes, Monthly Weather Review, 135, 1961–1973, 2007.

Parish, T. R. and Cassano, J. J.: Diagnosis of the katabatic wind influence on the wintertime Antarctic surface wind field from numerical simulations, Monthly Weather Review, 131, 1128–1139, 2003.

Pei, Z., Fiddes, S. L., French, W. J. R., Alexander, S. P., Mallet, M. D., Kuma, P., and McDonald, A.: Assessing the cloud radiative bias at Macquarie Island in the ACCESS-AM2 model, Atmospheric Chemistry and Physics, 23, 14 691–14 714, 2023.

Pei, Z., Fiddes, S. L., Mallet, M. D., Alexander, S. P., Furtado, K., Roff, G., Protat, A., McDonald, A., and French, W. J. R.: Simulating mixed-phase clouds over coastal Antarctica during a significant snowfall event in a high-resolution regional model, Journal of Geophysical Research: Atmospheres, 130, e2024JD042 311, 2025.

Pfitzenmaier, L., Unal, C. M., Dufournet, Y., and Russchenberg, H. W.: Observing ice particle growth along fall streaks in mixed-phase clouds using spectral polarimetric radar data, Atmospheric chemistry and physics, 18, 7843–7862, 2018.

Praz, C., Roulet, Y.-A., and Berne, A.: Solid hydrometeor classification and riming degree estimation from pictures collected with a Multi-Angle Snowflake Camera, Atmospheric Measurement Techniques, 10, 1335–1357, 2017.

Pruppacher, H. R., Klett, J. D., and Wang, P. K.: Microphysics of clouds and precipitation, 1998.

Rogers, R. and Yau, M.: A short course in cloud physics, Bull. Amer. Meteor. Soc, 45, 619.

Ryzhkov, A. V., Giangrande, S. E., Melnikov, V. M., and Schuur, T. J.: Calibration issues of dual-polarization radar measurements, Journal of Atmospheric and Oceanic Technology, 22, 1138–1155, 2005.

https://doi.org/10.5194/egusphere-2026-4159
Preprint. Discussion started: 13 August 2026

Schneebeli, M., Dawes, N., Lehning, M., and Berne, A.: High-resolution vertical profiles of X-band polarimetric radar observables during snowfall in the Swiss Alps, Journal of applied meteorology and climatology, 52, 378–394, 2013.

Schrom, R. S. and Kumjian, M. R.: Connecting microphysical processes in Colorado winter storms with vertical profiles of radar observations, Journal of Applied Meteorology and Climatology, 55, 1771–1787, 2016.

Schrom, R. S., van Lier-Walqui, M., Kumjian, M. R., Harrington, J. Y., Jensen, A. A., and Chen, Y.-S.: Radar-based Bayesian estimation of ice crystal growth parameters within a microphysical model, Journal of the Atmospheric Sciences, 78, 549–569, 2021.

Silva, T. and Schlosser, E.: A 25-year climatology of low-tropospheric temperature and humidity inversions for contrasting synoptic regimes at Neumayer Station, Antarctica, Weather and Climate Dynamics Discussions, 2021, 1–34, 2021.

Silva, T., Schlosser, E., and Lehner, M.: A 25-year climatology of low-tropospheric temperature and humidity inversions for contrasting synoptic regimes at Neumayer Station, Antarctica, International Journal of Climatology, 43, 456–479, 2023.

Silvano, A., Foppert, A., Rintoul, S. R., Holland, P. R., Tamura, T., Kimura, N., Castagno, P., Falco, P., Budillon, G., Haumann, F. A., et al.: Recent recovery of Antarctic Bottom Water formation in the Ross Sea driven by climate anomalies, Nature Geoscience, 13, 780–786, 2020.

Sinclair, V. A., Moisseev, D., and von Lerber, A.: How dual-polarization radar observations can be used to verify model representation of secondary ice, Journal of Geophysical Research: Atmospheres, 121, 10–954, 2016.

Skofronick-Jackson, G., Petersen, W. A., Berg, W., Kidd, C., Stocker, E. F., Kirschbaum, D. B., Kakar, R., Braun, S. A., Huffman, G. J., Iguchi, T., et al.: The Global Precipitation Measurement (GPM) mission for science and society, Bulletin of the American Meteorological Society, 98, 1679–1695, 2017.

Sotiropoulou, G., Vignon, É., Young, G., Morrison, H., O'Shea, S. J., Lachlan-Cope, T., Berne, A., and Nenes, A.: Secondary ice production in summer clouds over the Antarctic coast: an underappreciated process in atmospheric models, Atmospheric Chemistry and Physics, 21, 755–771, 2021.

Stephens, G. L., Vane, D. G., Boain, R. J., Mace, G. G., Sassen, K., Wang, Z., Illingworth, A. J., O'connor, E. J., Rossow, W. B., Durden, S. L., et al.: The CloudSat mission and the A-Train: A new dimension of space-based observations of clouds and precipitation, Bulletin of the American Meteorological Society, 83, 1771–1790, 2002.

Takahashi, T.: Influence of liquid water content and temperature on the form and growth of branched planar snow crystals in a cloud, Journal of the Atmospheric Sciences, 71, 4127–4142, 2014.

Takahashi, T. and Nagao, Y.: Possible high ice particle production during Graupel-Graupel collisions., Journal of the atmospheric sciences, 52, 1995.

Thorndike, R. L.: Who belongs in the family?, Psychometrika, 18, 267–276, 1953.

Tomikawa, Y., Nomoto, M., Miura, H., Tsutsumi, M., Nishimura, K., Nakamura, T., Yamagishi, H., Yamanouchi, T., Sato, T., and Sato, K.: Vertical wind disturbances during a strong wind event observed by the PANSY radar at Syowa Station, Antarctica, Monthly Weather Review, 143, 1804–1821, 2015.

Turner, J., Chenoli, S. N., Abu Samah, A., Marshall, G., Phillips, T., and Orr, A.: Strong wind events in the Antarctic, Journal of Geophysical Research: Atmospheres, 114, 2009.

Turner, J., Phillips, T., Thamban, M., Rahaman, W., Marshall, G. J., Wille, J. D., Favier, V., Winton, V. H. L., Thomas, E., Wang, Z., et al.: The dominant role of extreme precipitation events in Antarctic snowfall variability, Geophysical Research Letters, 46, 3502–3511, 2019.

Vardiman, L.: The generation of secondary ice particles in clouds by crystal–crystal collision, Journal of Atmospheric Sciences, 35, 2168–2180, 1978.

https://doi.org/10.5194/egusphere-2026-4159
Preprint. Discussion started: 13 August 2026

Vignon, É., Traullé, O., and Berne, A.: On the fine vertical structure of the low troposphere over the coastal margins of East Antarctica, Atmospheric Chemistry and Physics, 19, 4659–4683, 2019.

Vignon, É., Alexander, S., DeMott, P., Sotiropoulou, G., Gerber, F., Hill, T., Marchand, R., Nenes, A., and Berne, A.: Challenging and improving the simulation of mid-level mixed-phase clouds over the high-latitude Southern Ocean, Journal of Geophysical Research: Atmospheres, 126, e2020JD033 490, 2021.

Vogel, J. M. and Fabry, F.: Contrasting polarimetric observations of stratiform riming and nonriming events, Journal of Applied Meteorology and Climatology, 57, 457–476, 2018.

Wiener, V., Roussel, M.-L., Genthon, C., Vignon, É., Grazioli, J., and Berne, A.: A 7-year record of vertical profiles of radar measurements and precipitation estimates at Dumont d'Urville, Adélie Land, East Antarctica, Earth System Science Data, 16, 821–836, 2024.

https://doi.org/10.5194/egusphere-2026-4159
Preprint. Discussion started: 13 August 2026

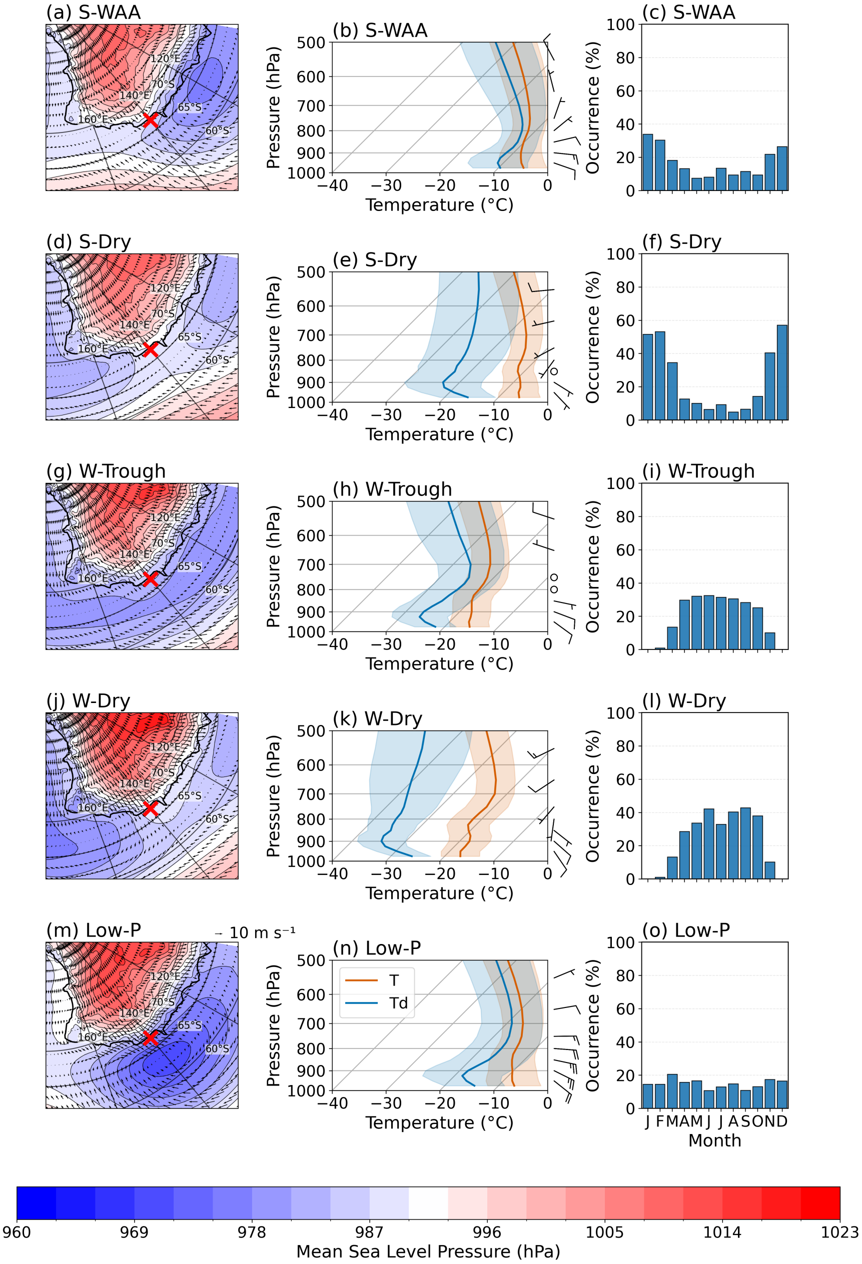

Figure 1. Characteristics of synoptic regimes at Dumont d'Urville (DDU). (a, d, g, j, m) Spatial distributions of mean sea-level pressure (MSLP; hPa) and 10 m wind vectors (m s^{-1}) over East Antarctica for the five major synoptic types identified at DDU during 2015–2023. The red marker indicates the location of DDU (66.6°S, 140°E). (b, e, h, k, n) Composite Skew-T–log$p$ thermodynamic diagrams for each synoptic type at DDU, derived from ERA5. The red and green lines show the mean temperature and dew-point temperature profiles, respectively, while the shaded regions denote one standard deviation. Wind barbs on the right indicate wind speed and direction at the corresponding pressure levels. (c, f, i, l, o) Seasonal distributions of the synoptic regimes at DDU.

https://doi.org/10.5194/egusphere-2026-4159
Preprint. Discussion started: 13 August 2026

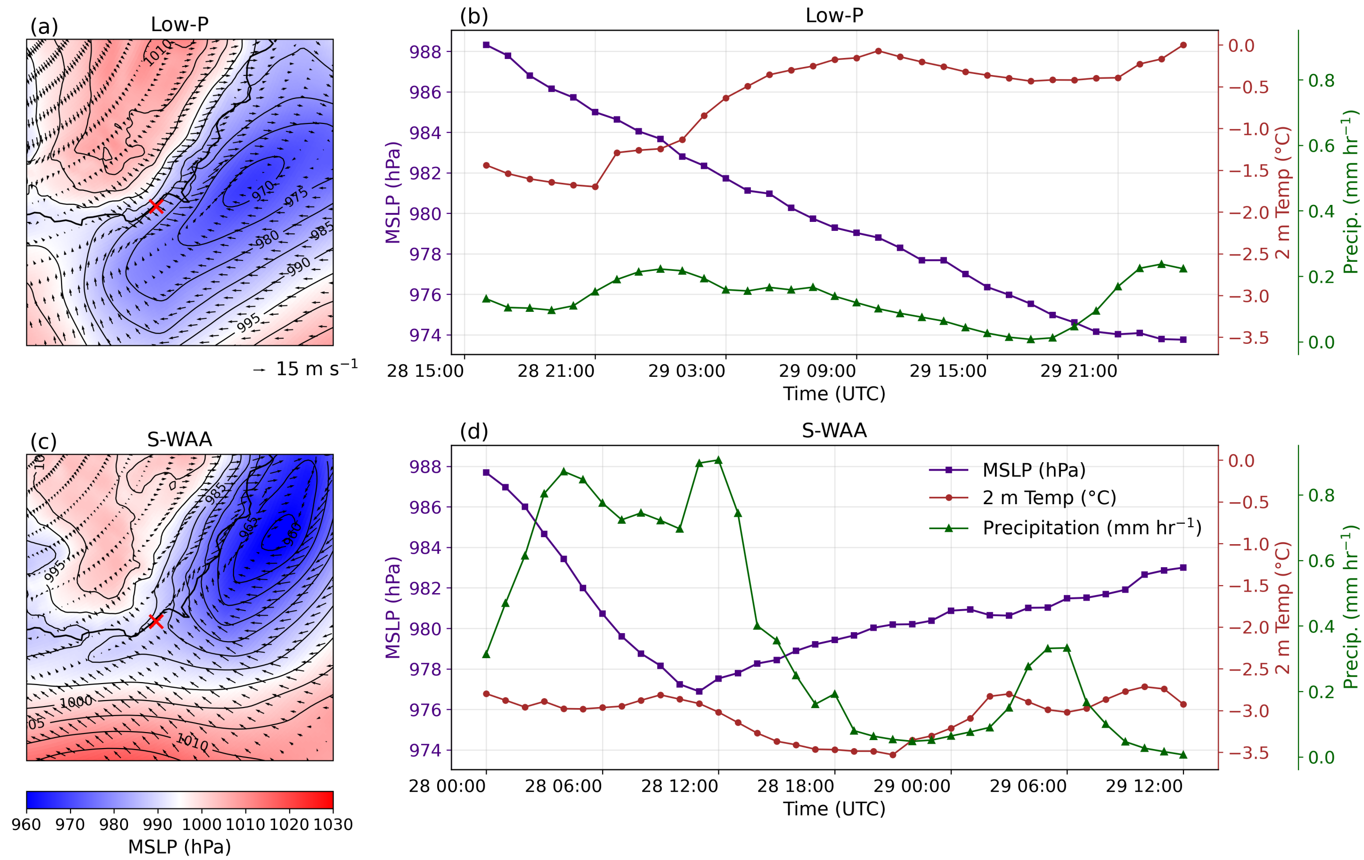

Figure 2. Circulation and surface meteorology at DDU during Low-P and S-WAA cases: (a) Composite mean fields of MSLP and 10 m winds during the Low-P case study (16:00 UTC on 28 December 2015 to 00:00 UTC on 30 December 2015), calculated over the duration of the event. The red marker indicates the location of DDU (66.6°S, 140°E). (b) Time series of MSLP, 2 m temperature, and precipitation at DDU from ERA5 during the Low-P case. (c) Same as (a), but for the S-WAA case (00:00 UTC on 28 January 2016 to 12:00 UTC on 29 January 2016). (d) Same as (b), but for the S-WAA case.

https://doi.org/10.5194/egusphere-2026-4159
Preprint. Discussion started: 13 August 2026

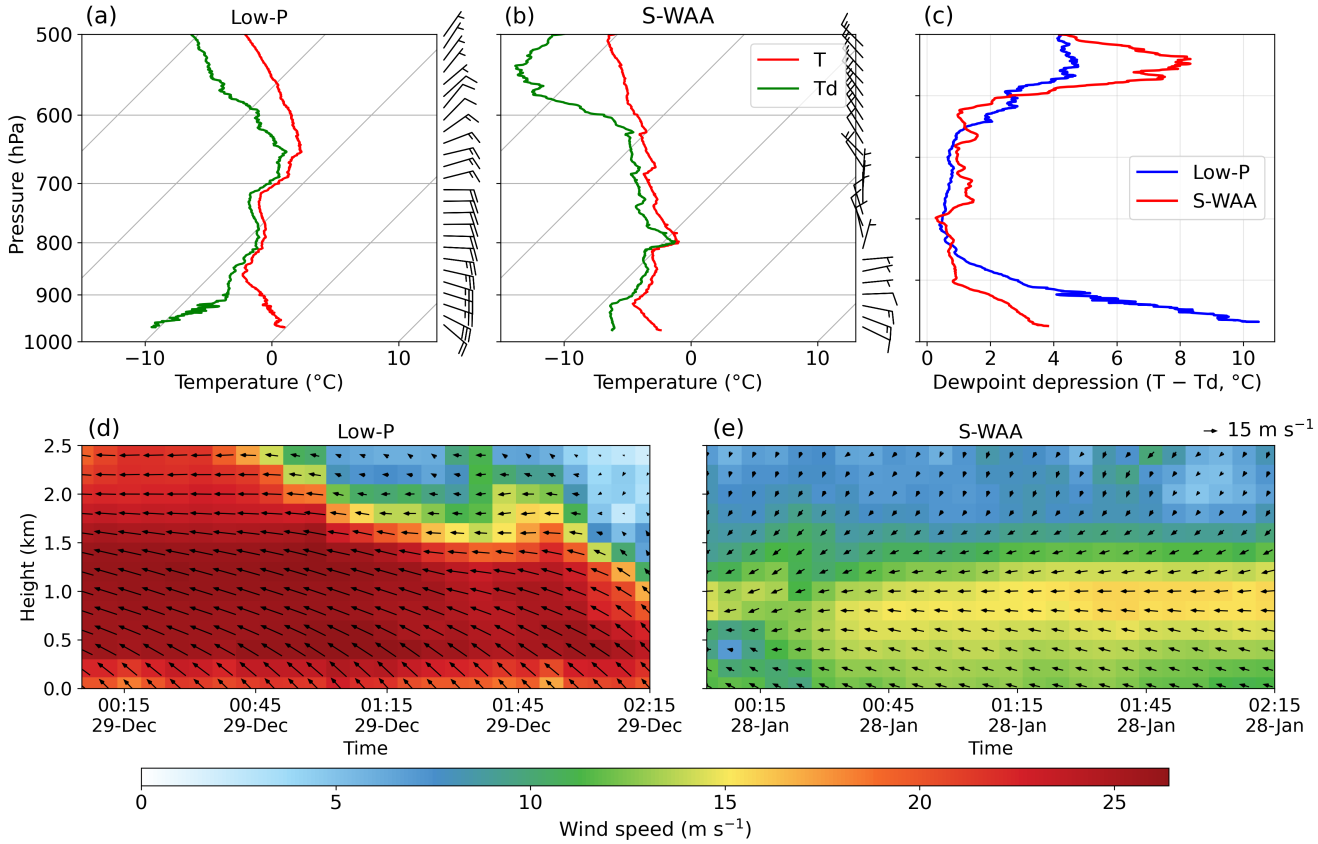

Figure 3. Skew-T–log$p$ from radiosonde and VAD profiles from X-band radar. (a) Skew-T–log$p$ diagram for the Low-P event at DDU, computed based on the radiosonde launched at 00:00 UTC on 29 December 2015. (b) Same as (a), but for the S-WAA event, based on the radiosonde launched at 00:00 UTC on 28 January 2016. (c) Vertical profiles of dewpoint depression for the Low-P (solid blue line) and S-WAA (solid red line) events. (d) Velocity–azimuth display (VAD) from X-band dual-polarization radar observations during the Low-P event, showing the vertical structure of horizontal wind speed and direction. (e) Same as (d), but for the S-WAA event.

https://doi.org/10.5194/egusphere-2026-4159
Preprint. Discussion started: 13 August 2026

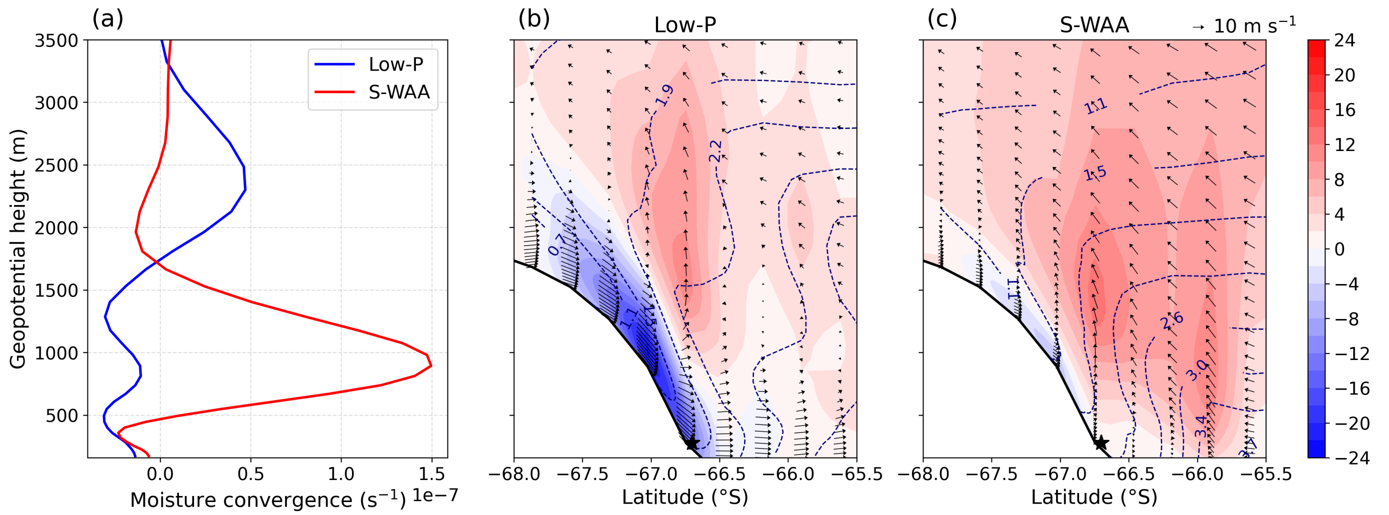

Figure 4. Moisture convergence and vertical circulation from ERA5. (a) Vertical profiles of moisture convergence (s^{-1}) during the Low-P (29 December 2015) and S-WAA (28 January 2016) events, evaluated at the ERA5 grid point nearest to DDU for the period 00:00–03:00 UTC. (b) Meridional cross-section of vertical velocity (w, m s^{-1}; shaded) along 140°E, with meridional–vertical wind vectors (v, w) overlaid and w scaled by a factor of 100. Blue dotted contours denote specific humidity (q, g kg^{-1}). The black star marks DDU, and the solid black line represents the underlying orography (m). (c) Same as (b), but for the S-WAA event.

https://doi.org/10.5194/egusphere-2026-4159
Preprint. Discussion started: 13 August 2026

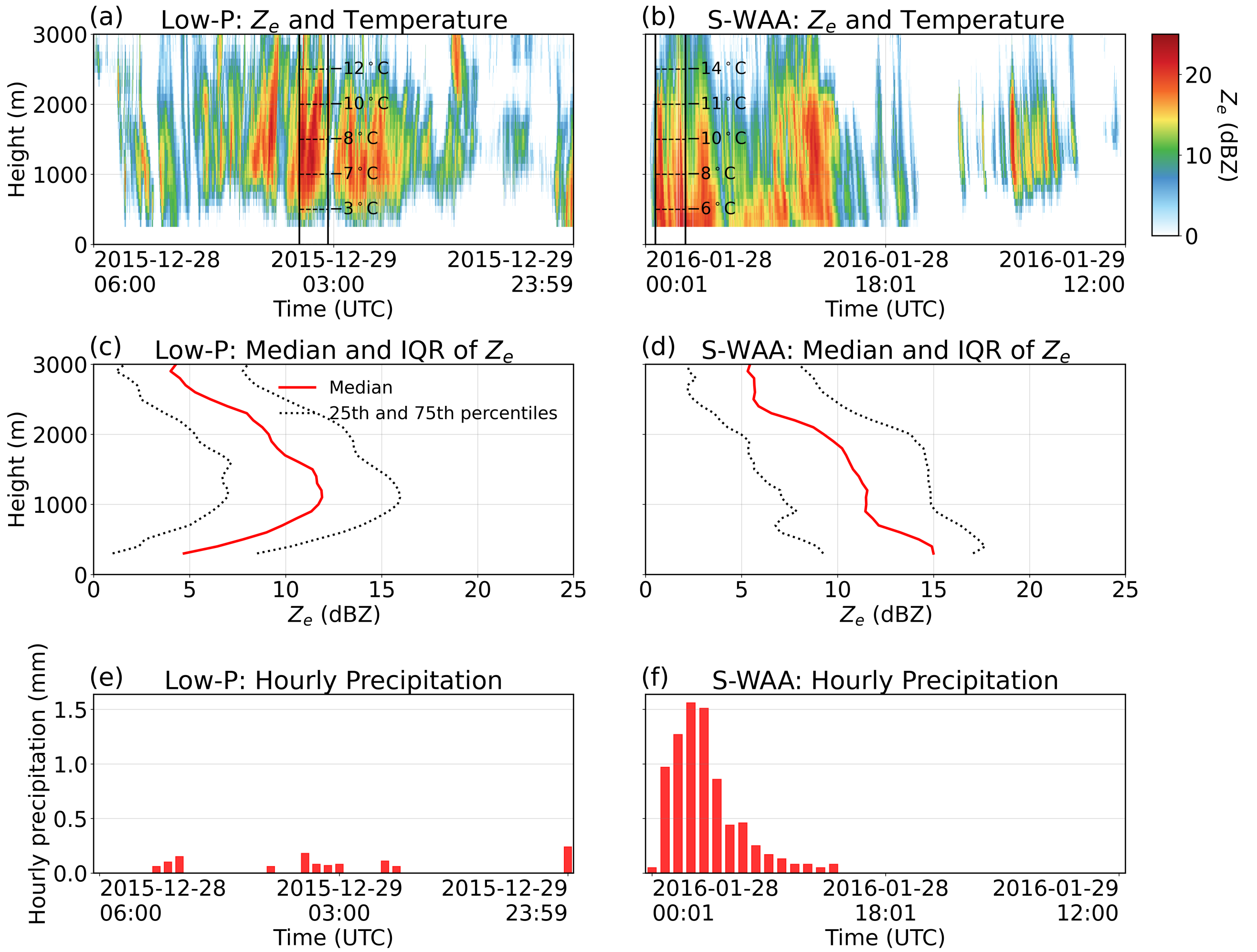

Figure 5. Precipitation evolution from MRR and OTT Pluvio: (a) Time–height cross-section of equivalent radar reflectivity (Z_e) observed by the MRR during the Low-P event at DDU. Temperature contours are derived from the radiosonde launched at 00 UTC on 29 December 2015. The period from 00:00 to 03:00 UTC on 29 December 2015 is indicated by the black vertical lines. (b) Same as (a), but for the S-WAA event, with temperature contours derived from the radiosonde launched at 00 UTC on 28 January 2016. The period from 00:00 to 03:00 UTC on 28 January 2016 is indicated by the black vertical lines. (c) Vertical profiles of the median (solid) and the 25^{th} and 75^{th} percentiles (dotted) of Z_e for the Low-P event, computed over 00–03 UTC on 29 December 2015. (d) Same as (c), but for the S-WAA event, computed over 00–03 UTC on 28 January 2016. (e) Time series of surface precipitation rate measured by the OTT Pluvio^2 during the Low-P event. (f) Same as (e), but for the S-WAA event.

https://doi.org/10.5194/egusphere-2026-4159
Preprint. Discussion started: 13 August 2026

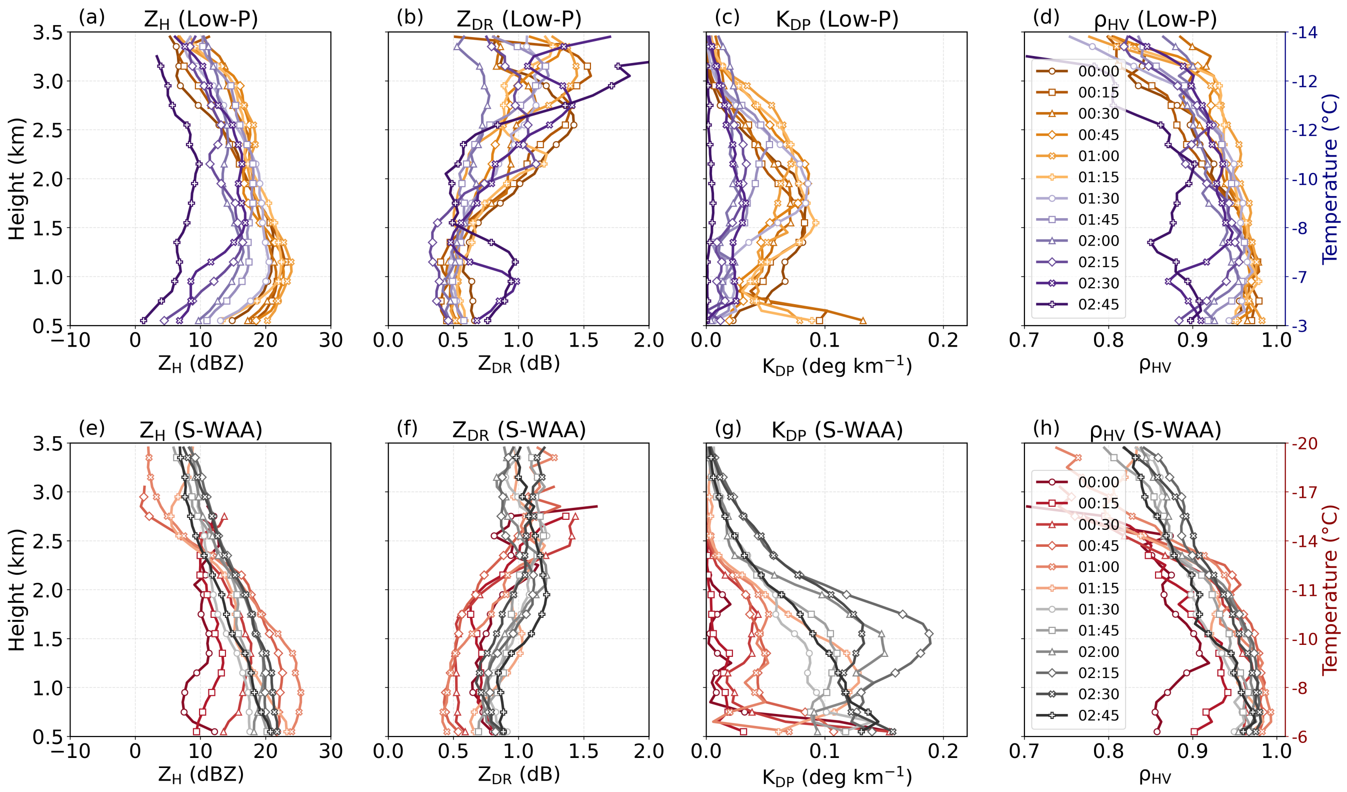

Figure 6. Polarimetric signatures of hydrometeor growth: (a–d) Vertical profiles of (a) reflectivity (Z_H), (b) differential reflectivity (Z_{DR}), (c) specific differential phase (K_{DP}), and (d) copolar correlation coefficient (ρ_{HV}) derived from MXPol radar observations during the Low-P case at DDU. Profiles are shown for the period 00:00–03:00 UTC on 29 December 2015 as 15-minute averages, using elevation angles below 40°. The secondary y-axis (blue) shows the temperature profile from radiosonde measurements at 00:00 UTC on 29 December 2015. (e–h) Same as (a–d), but for the S-WAA case, with profiles shown for 00:00–03:00 UTC on 28 January 2016 as 15-minute averages. The secondary y-axis (red) shows the temperature profile from radiosonde measurements at 00:00 UTC on 28 January 2016.

https://doi.org/10.5194/egusphere-2026-4159
Preprint. Discussion started: 13 August 2026

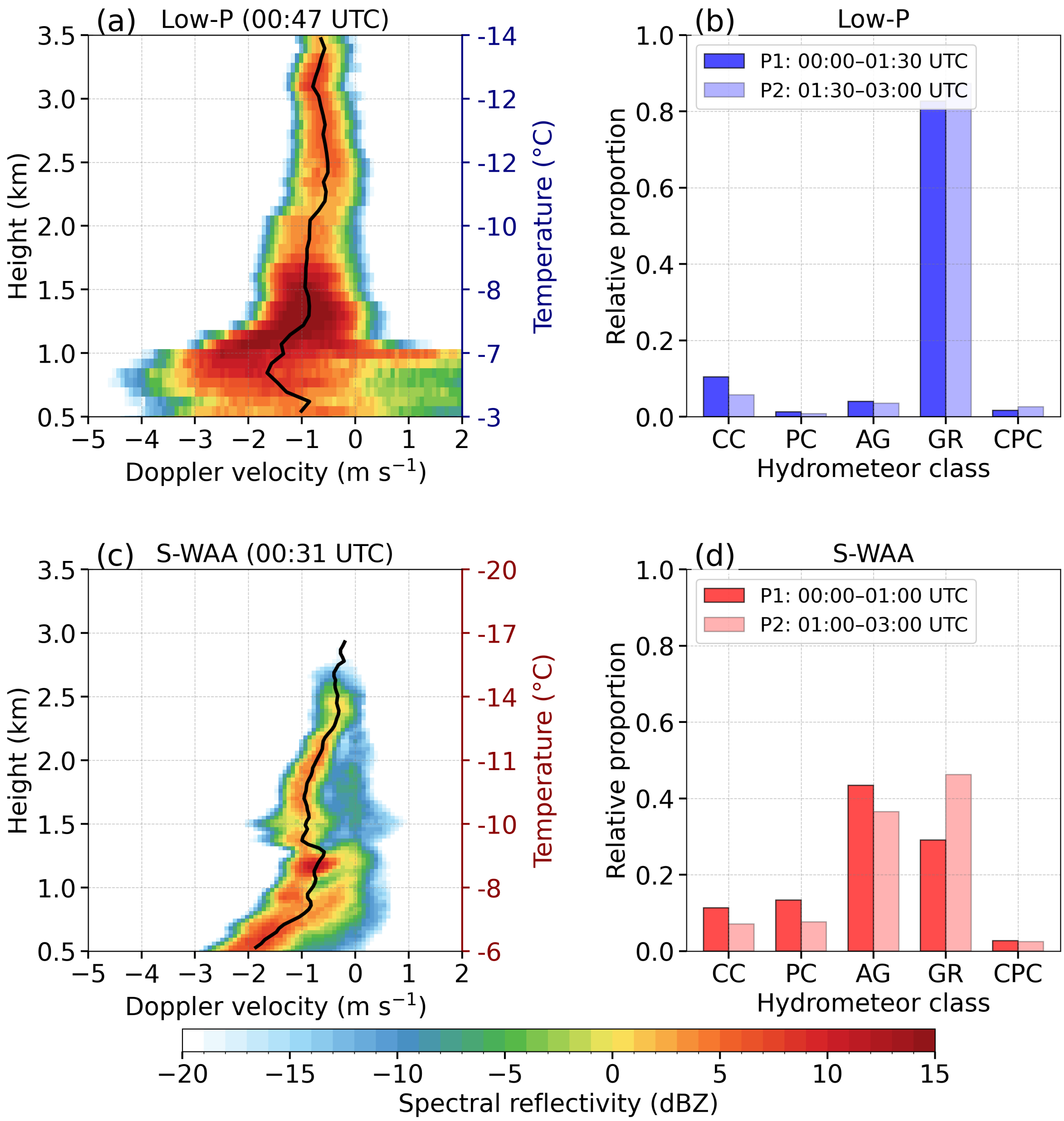

Figure 7. Doppler Spectrograms and MASC Hydrometeors: (a) Doppler spectrogram for the Low-P case at 00:47 UTC on 29 December 2015. The mean Doppler velocity is indicated by the solid black line. (b) Relative contributions of hydrometeor types to the total particle population during the Low-P event (00:00–03:00 UTC on 29 December 2015). (c) Same as panel (a), but for the S-WAA case at 00:31 UTC on 28 January 2016. (d) Same as panel (b), but for the S-WAA event (00:00–03:00 UTC on 28 January 2016). Hydrometeor classes include columnar crystals (CC), planar crystals (PC), aggregates (AG), graupel (GR), and combined columnar and planar crystals (CPC). The selected periods (P1 and P2) are characterised by similar polarimetric signatures (Fig. 6).

https://doi.org/10.5194/egusphere-2026-4159
Preprint. Discussion started: 13 August 2026

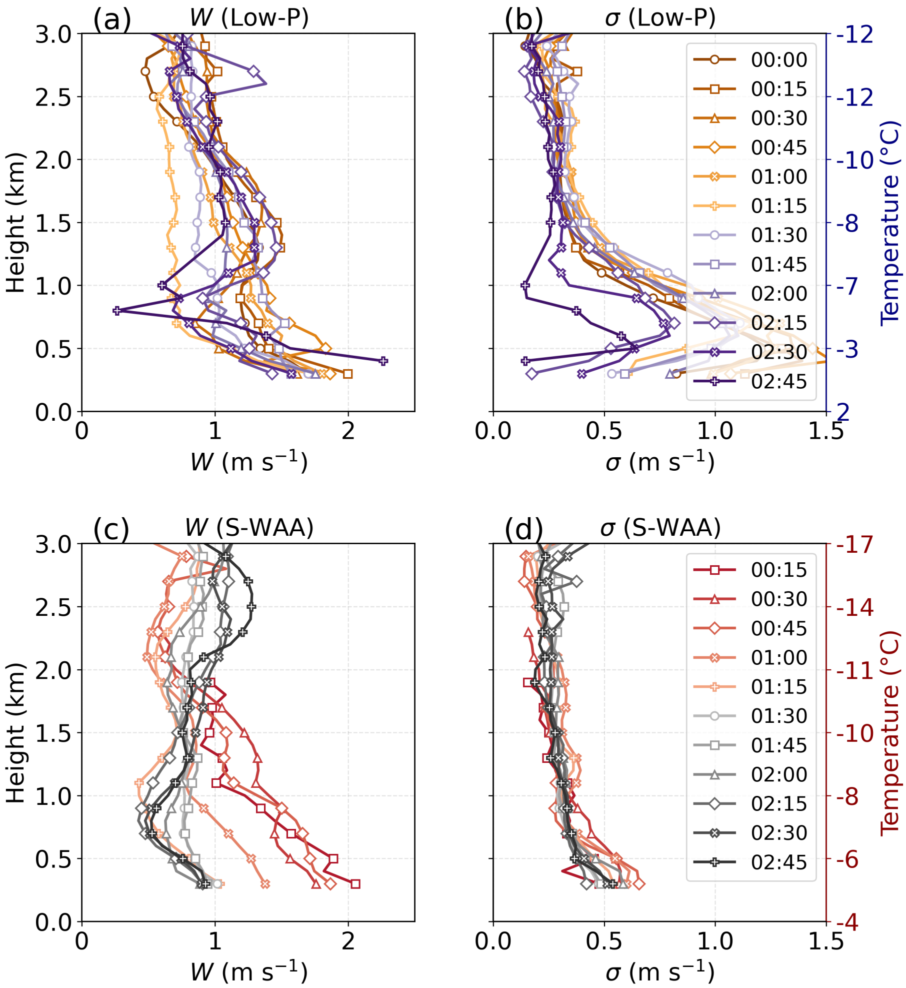

Figure 8. Vertical structure of Doppler velocity and spectral width: (a, d) Time–height cross-sections of (a) Doppler velocity (W, m s^{-1}) and (b) spectral width (σ, m s^{-1}) observed by the MRR during the Low-P case at DDU from 00:00 to 03:00 UTC on 29 December 2015. The profiles represent 15-minute averaged values. (c–d) Same as (a–b), but for the S-WAA case from 00:15 to 03:00 UTC on 28 January 2016.

https://doi.org/10.5194/egusphere-2026-4159
Preprint. Discussion started: 13 August 2026

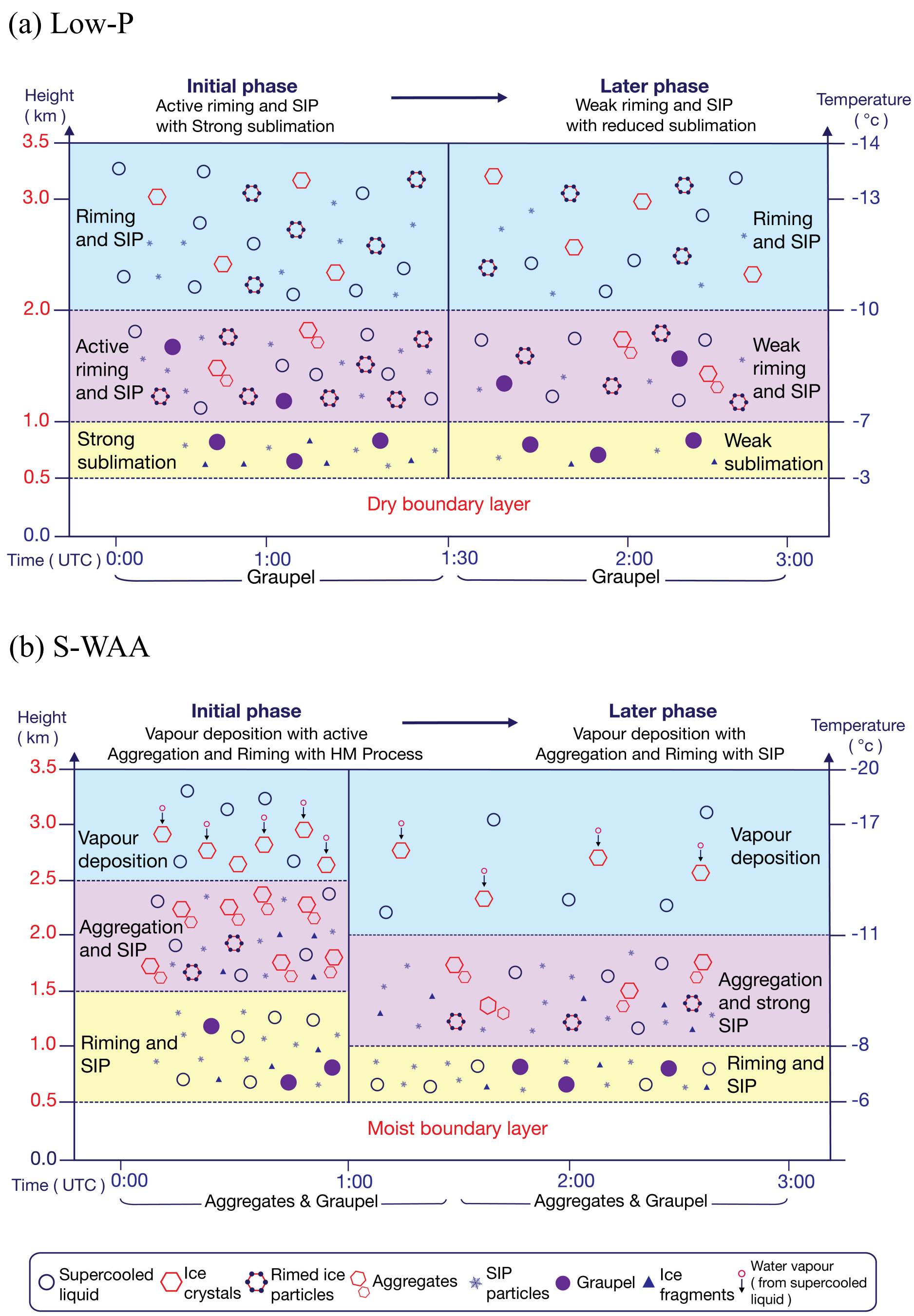

Figure 9. Schematic of hydrometeor growth processes: Schematic representation of cloud microphysical processes during (a) the Low-P case and (b) the S-WAA case at DDU. The two phases of cloud growth, distinguished by their polarimetric signatures, are presented separately.

https://doi.org/10.5194/egusphere-2026-4159
Preprint. Discussion started: 13 August 2026

Level	Variables
Surface and 2 m	Surface pressure (SP), 2-m air temperature (T_{2m}), 2-m relative humidity (RH_{2m})
700, 850, and 925 hPa	Temperature (T), relative humidity (RH), zonal wind (u), and meridional wind (v)

Table 1. Variables used in the K-means clustering analysis.

Regime	Total-Obs (mm)	Total-ERA5 (mm)	Mean-Obs (mm hr^{-1})	Mean-ERA5 (mm hr^{-1})	r
S-WAA	2408.2	2288.8	0.21	0.20	0.56*
S-Dry	15.7	6.0	0.00	0.00	-0.04
W-Trough	252.0	183.4	0.02	0.02	0.36*
W-Dry	23.6	0.2	0.00	0.00	-0.07
Low-P	2327.9	1205.9	0.28	0.15	0.37*
Total	5027.4	3684.1	0.08	0.06	0.45*

Table 2. Comparison of observed and ERA5 precipitation statistics for the identified synoptic regimes at DDU. Asterisks indicate statistically significant correlations ($p < 0.05$).